PCCP

Accepted Manuscript

This is an *Accepted Manuscript*, which has been through the Royal Society of Chemistry peer review process and has been accepted for publication.

Accepted Manuscripts are published online shortly after acceptance, before technical editing, formatting and proof reading. Using this free service, authors can make their results available to the community, in citable form, before we publish the edited article. We will replace this *Accepted Manuscript* with the edited and formatted *Advance Article* as soon as it is available.

You can find more information about *Accepted Manuscripts* in the Information for Authors.

Please note that technical editing may introduce minor changes to the text and/or graphics, which may alter content. The journal's standard Terms & Conditions and the Ethical guidelines still apply. In no event shall the Royal Society of Chemistry be held responsible for any errors or omissions in this *Accepted Manuscript* or any consequences arising from the use of any information it contains.

ROYAL SOCIETY OF CHEMISTRY

www.rsc.org/pccp

Expansion dynamics of supercritical water probed by picosecond time-resolved photoelectron spectroscopy

Thomas Gladytz[a,b], Bernd Abel[a,b] and Katrin R. Siefermann[a,*]

[a] Leibniz-Institute of Surface Modification (IOM), Chemistry Department, Permoserstr. 15, 04318 Leipzig, Germany

[b] University of Leipzig, Wilhelm-Ostwald-Institute for Physical and Theoretical Chemistry, Linnéstr. 3, 04318 Leipzig, Germany

* corresponding author: katrin.siefermann@iom-leipzig.de

TOC Abstract

A combined experimental and theoretical study delivers a nanoscale picture on the picosecond expansion dynamics of supercritical water into vacuum. The study covers a time-resolved photoelectron spectroscopy experiment on a liquid water microjet, analysis of experimental data with a specifically developed multivariate method, and simulations based on a fluid dynamics simulation.

Keywords

supercritical water, vibrational excitation, ultrafast, time-resolved spectroscopy, photoelectron spectroscopy, liquid jet, chemometrics, multivariate curve resolution, complex mixture spectra, hybrid hard and soft modelling, target transform fitting, fluid dynamics, expansion wave

Physical Chemistry Chemical Physics Accepted Manuscript

Abstract

Vibrational excitation of liquid water with femtosecond laser pulses can create extreme states of water. Yet, the dynamics directly after initial sub-picosecond delocalization of molecular vibrations remain largely unclear. We study the ultrafast expansion dynamics of a respectively prepared supercritical water phase for timescales between 1 ps and several 100 ps. Our experimental setup combines liquid micro-jet technology in vacuum and a table top High Harmonic light source driven by a femtosecond laser system. An ultrashort laser pulse centered at a wavelength of 2900 nm excites the OH-stretch vibration of water molecules in the liquid. The deposited energy corresponds to a supercritical phase with a temperature of about 1000 K and a pressure of more than 1 GPa. We use a time-delayed extreme ultraviolet pulse centered at 38.6 eV, and obtained via High Harmonic generation (HHG), to record valence band photoelectron spectra of the expanding water sample. The series of photoelectron spectra is analyzed with noise-corrected target transform fitting (cTTF), a specifically developed multivariate method. Together with a simple fluid dynamics simulation, the following picture emerges: When a supercritical phase of water expands into vacuum, temperature and density of the first few nanometers of the expanding phase drop below the critical values within a few picoseconds. This results in a supersaturated phase, in which condensation seeds form and grow from small clusters to large clusters on a 100 picosecond timescale.

Physical Chemistry Chemical Physics Accepted Manuscript

1 Introduction

Water remains a subject of high scientific interest, in particular with respect to its microscopic structure[1–4] and its surface properties[5–7]. In recent years, ultrafast dynamics in bulk water and on water surfaces and interfaces moved into the focus of numerous experimental and theoretical investigations[8–12]. Ultrafast timescales are of interest, since they capture changes on the molecular scale. They ultimately provide a possibility to connect changes on the molecular level to changes observed on the macroscopic scale. A topic of continued interest is the question of energy deposition and redistribution on ultrafast timescales, as well as the subsequent behavior (e.g. expansion) of the hot water phase. When energy is deposited in a vibrational mode of a water molecule, ultrafast experiments revealed that vibrational couplings govern energy relaxation in water. They further demonstrate that molecular vibrations are delocalized via intermolecular couplings on sub-picosecond timescales[8,9,13,14], even for vibrationally excited surface water molecules[11]. This indicates that thermalization in water is ultrafast and completed within several ps. This even holds for energy delocalization in a superheated water environment[15], and for deposited energy densities corresponding to temperatures of 2000°C[16]. Taken together, these experiments provide various information on the initial energy delocalization after vibrational excitation of liquid water.

However, the dynamics taking place directly after energy deposition and delocalization remain largely unclear. On these timescales (> 1 ps) translational motion plays a role and the liquid ensemble is able to adjust to the energy input. Of particular interest is the situation in which the liquid has the possibility to expand into air or vacuum subsequent to the energy deposition via vibrational excitation of the water. For this

Physical Chemistry Chemical Physics Accepted Manuscript

Physical Chemistry Chemical Physics Accepted Manuscript

case, information for the initial timescale between 1 ps and 100 ps is limited to a few studies without providing a complete picture on mechanism and timescales. These studies are time-resolved photoelectron spectroscopy experiments on a liquid water jet in vacuum by the Abel group[17–20]. While these experiments delivered first insights into the ultrafast dynamics of the expanding phase, a major hurdle for interpretation of the experimental data was the strong overlap of signals in the photoelectron spectra. In the work presented here, we have cleared this hurdle by analysis of the experimental data with a specifically developed multivariate method and interpretation of obtained results with a fluid dynamics simulation. The result is a detailed and comprehensive picture on the involved states of water and their concentration profiles as a function of time.

With this we provide a link between ultrafast energy relaxation experiments of vibrationally excited water molecules taking place on the 1 ps timescale and experiments on the macroscopic expansion of a highly excited thermodynamic water phase at the water/air interface reported for timescales > 100 ps[21]. For timescales > 100 ps, the recent study by Franjic and Miller[21] provides detailed experimental data on the formation of the expansion plume and a description by an ablation model.

With this, a picture emerges which ranges from the energy deposition and delocalization on a molecular level to the macroscopically observable ablation of water. This information is relevant for the ablation of biological tissue in laser surgery[22],for matrix-assisted laser desorption/ionization (MALDI) from water ice matrices[23,24], and laser induced liquid beam ionization/desorption (LILBID) mass spectrometry[25,26] as these techniques rely on this basic principle. In LILBID, the aqueous sample solution is injected into vacuum as a liquid jet[25,26] or into air as droplets[27]. It is intersected with an infrared laser, which deposits energy into the vibrational modes of water and thus leads to dispersion of the sample and soft release of dissolved molecules for subsequent mass spectroscopic investigation.

2 Experimental

The general experimental setup for time-resolved photoelectron spectroscopy on a liquid microjet is described in Ref. [17–20]. For the present experiment, we split pump and probe pulse inside the femtosecond laser system (Spectra Physics, Hurricane, 1 kHz, $\lambda c = 800$ nm) between regenerative amplifier and compressor unit. The probe pulse (380 µJ) leaves the femtosecond laser system uncompressed. It is sent into a home built three pass amplifier unit pumped by a Nd:YAG laser (ORC1000, Clark-MXR, 532 nm, 8 W). After a home built grating compressor we detect a pulse energy of 1.25 mJ at a central wavelength of 800 nm and a pulse length of 110 fs. A lens (f = 200 mm) focuses the beam for high harmonic generation in a capillary (diameter 3 mm) filled with Argon gas. The pressure in the interaction region is estimated to 50 – 100 mbar. A 150 nm thick aluminum filter (Luxel) blocks the 800 nm fundamental. It is installed between the HHG chamber and the subsequent grating chamber. The grating (700 groves/mm, radius 17100 mm, blaze angle 1.7°) is oriented such that the 25th harmonic (38.7 eV, 32 nm) is directed onto a toroidal mirror (Au, R1 = 24.1 mm, R2 = 5375.3 mm), which focuses it onto the liquid jet sample. The focus is somewhat asymmetric with a full width at half maximum (FWHM) of about 100 µm. We estimate the number of extreme ultraviolet (XUV) photons in the focus to be on the order of 10^4 to 10^5 photons/pulse. The pump pulse leaves the femtosecond laser system with 780 µJ/pulse and a pulse length of 100 fs. After passing the delay stage, 670 µJ/pulse

Physical Chemistry Chemical Physics Accepted Manuscript

Physical Chemistry Chemical Physics Accepted Manuscript

are coupled into an optical parametric amplifier (TOPAS, Light Conversion). The TOPAS is optimized to deliver ~1100 nm as the signal wavelength. Difference frequency mixing with residual 800 nm in a 5 mm long KTP (potassium titanyl phosphate) crystal yields pulses at a wavelength of 2900 nm and a pulse length on the order of 250 fs[28]. A prism (Infrasil) is used to separate 2900 nm from the fundamental 800 nm and the residual signal wave at 1100 nm. At the sample position we detect pulse energies of ~20 µJ. The light is focused by an off axis parabolic mirror (f = 34 mm) onto the liquid jet yielding a focus diameter of about 100 µm. The cross correlation signal between IR-pump and XUV-probe pulse has a FWHM of 530 fs.

A HPLC-pump injects the liquid through a quartz nozzle into vacuum (flux rate of 0.4 ml/min). The nozzles have typical opening diameters of about 20 µm, producing liquid jets with diameters of about 16 µm. The temperature of the liquid at a distance of 2 mm from the nozzle is estimated to 263 K[20].

Photoelectrons pass a 100-150 µm skimmer, at a distance of about 500 µm to the liquid jet, to enter the time-of-flight photoelectron spectrometer. Photoelectron count rates in the water spectrum are between 250 - 500 counts/second. The TOF data are converted into binding energies with a calibration function, so that binding energies of photoelectron signals match those reported in literature[29,30]. Details on data treatment are presented in the supporting information S1.

3 Results

a) Experimental Data:

Light with a wavelength of 2900 nm is in resonance with the OH stretch vibration in liquid water and thus absorption coefficients are high $\alpha = 11768\ \mathrm{cm}^{-1}$.[31] We estimate the energy density deposited in the liquid jet as follows: The IR pulse (20 µJ) in the focus is assumed to be Gaussian with a FWHM of 100 µm and hits the jet (diameter = 16 µm) perpendicular to its flow axis. In the case of ideal alignment of IR focus and jet, the light is thus absorbed on an area of about 16 x 100 um^2. This corresponds to the deposition of about 25% of the pulse energy in the liquid jet. We note that the intensity in the focus is about $1x10^{12}$ W/cm^2 and thus below the threshold for plasma formation[32]. The energy deposited within the first 10 nm of the jet (> probing depth in our experiment) is distributed homogeneously in good approximation, as only 1.17 % of the light is absorbed over this distance[31]. With this, we estimate the energy density in this volume (16 x 100 x 0.01 um^3) to 50 kJ/mol. Formally, this corresponds to more than one IR photon per water molecule. Although multiphoton absorption is possible, we continue our estimate with the conservative assumption that every water molecule only absorbs one IR-photon. This corresponds to a deposited energy of about 40 kJ/mol. Within the short time of energy deposition (250 fs), the water sample volume cannot significantly expand. Assuming constant volume over the time of energy deposition, the deposited energy (40 kJ/mol) directly corresponds to the change in internal energy $dU = c_V(T)\,dT$. The NIST Chemistry Webbook[33,34] provides the required thermophysical properties of water over a large temperature and pressure range. For a start temperature of 263 K and a start density of 1 g/ml, a change in internal energy by 40 kJ/mol results in a final temperature of about 1000 K[35]. The rapid increase in temperature is directly connected to a rapid increase in pressure, transferring the system into a supercritical state ($T = 1000\ K > Tc = 647\ K$, $p > 1\ GPa > pc = 22\ MPa$). We note that estimation of the start temperature remains a point of uncertainty and the actual temperature might deviate by as much as ± 100 K.

Physical Chemistry Chemical Physics Accepted Manuscript

Physical Chemistry Chemical Physics Accepted Manuscript

Figure 1 shows series of photoelectron spectra recorded at various time-delays between IR-pump and XUV-probe pulse. The XUV probe pulse ionizes the liquid sample and generates photoelectrons from the valence orbitals of the liquid and some gas phase around the liquid microjet. To illustrate liquid and gas phase contribution to the jet spectrum, Figure S1 in the supporting information shows a photoelectron spectrum recorded on the liquid jet and a pure gas phase spectrum. Photoelectron signals of liquid water are significantly broader and shifted towards lower binding energies with respect to the corresponding gas phase[30]. We note that spectra obtained in our static measurements (Figure S1) or performed with synchrotron light sources[29] exhibit a higher spectral resolution.

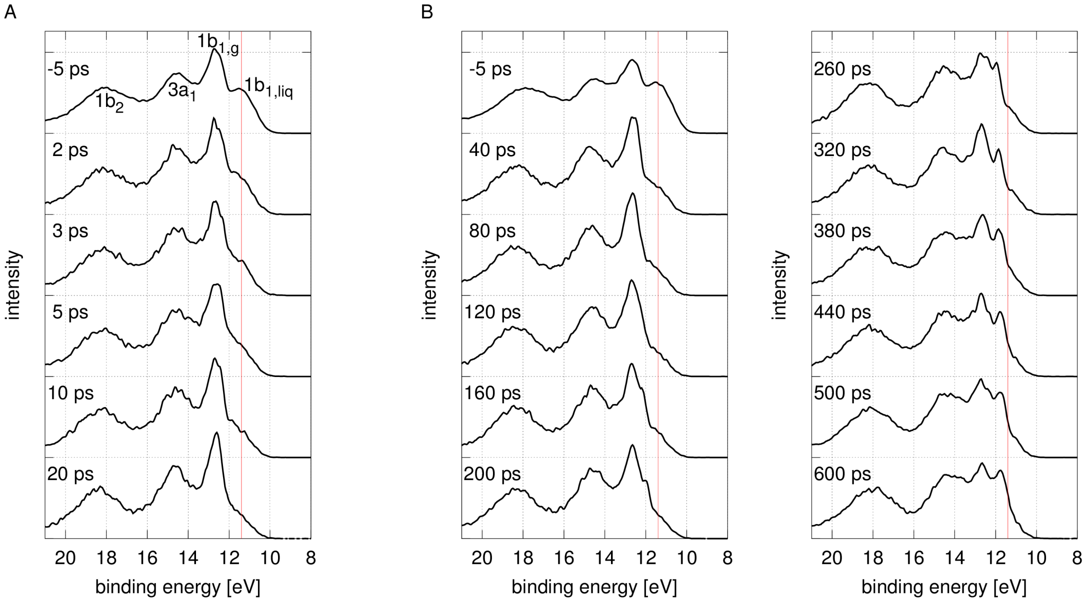

Figure 1:Series of photoelectron spectra of a liquid water jet at various time delays after excitation of the OH stretch vibration of water molecules by an IR -pump pulse at 2900 nm. The first spectrum in A) and B) is a reference spectrum of the unexcited sample, recorded at a time delay of -5 ps. 1A) displays spectra at short time delays, 1B) at longer time delays.

The first spectrum in Figure 1A and 1B, respectively, was recorded at a negative time delay of -5ps. In this case, the probe-pulse precedes the pump-pulse by 5 ps. The spectrum is identical to spectra recorded without the pump-pulse. The evolution of gas and liquid phase signal as a function of pump-probe delay is best followed by looking at the intensity of the signals labeled $1b_{1,g}$ and $1b_{1,liq}$. These photoelectron signals originate from the highest occupied molecular orbital (HOMO) of liquid and gas phase, respectively, and their signals are at least somewhat separated from signals from the lower lying valence states ($3a_1$, $1b_2$). The vertical red line indicates the position of the initial $1b_{1,liq}$ signal. Figure 1A shows how this signal changes on the timescale up to 20 ps. Figure 1B shows the evolution of the signal for longer time delays up to 500 ps. We note three points here: (1) Already the spectra at 2 ps and 5 ps show a shift of the center of the $1b_{1,liq}$ signal towards higher binding energies; this signal changes from a separate signal into a shoulder on the $1b_{1,g}$ signal. (2) Besides, the intensity of the $1b_{1,liq}$ signal decreases with increasing time delay. A minimum is reached at approx. 100 ps. (3) A new signal appears at a time delay of 160 ps and becomes more and more pronounced with increasing time delay. Comparison with the initial spectrum reveals that the new signal is different from the $1b_{1,liq}$ signal with regard to position and shape. We attribute the new signal to water clusters[36–38].

b) Noise-corrected target transform fitting (cTTF)

The series of photoelectron spectra presented in Figure 1 allow interesting insights into the picosecond expansion dynamics of supercritical water. However, the overlap of photoelectron signals originating from gas, clusters and liquid makes quantitative information challenging to obtain. To overcome this challenge, we developed the multivariate method "noise-corrected target transform fitting" (cTTF) with the goal to

Physical Chemistry Chemical Physics Accepted Manuscript

Physical Chemistry Chemical Physics Accepted Manuscript

deconvolute each spectrum of the series. In general, assuming that every spectrum (of a series of spectra) is a superposition of pure component spectra, the cTTF method delivers the number of involved components, their individual spectra, and information on how the ratio of these components changes over the series of spectra.

We note that attempts to obtain this information with established algorithms, such as hybrid MCR–ALS[39,40], have not been successful. The pure component spectra obtained with hybrid MCR-ALS contained spectral features of mixture spectra, indicating that the algorithm got trapped in a local minimum or a flat area and did not converge.

The cTTF method is an advanced version of target transform fitting (TTF) which was introduced by Jandanklang *et al.*[41]. TTF is a combination of target factor analysis with non-linear data fitting and is a powerful method to deconvolute complex spectra. However, TTF is challenged by the presence of components with low abundance and overlapping spectral features with low signal-to-noise ratios, as present in our series of spectra (Figure 1). We therefore developed a noise-correction algorithm and included it into the TTF routine. The resulting noise-corrected target transform fitting (cTTF) method is found to improve reliability of results.

The TTF method is described in detail by Jandanklang *et al.*[41]. As it is the basis of cTTF, we briefly summarize its principles (Figure 2).

TTF requires bilinearity, meaning that all spectra of a dataset are linear combinations of a limited number of pure component spectra. Accordingly, there is a high degree of correlation among the spectra of the dataset. Principal Component Analysis (PCA)[42] is used to identify this correlation in order to reduce complexity in the representation of the dataset (Figure 2, and supporting information S3). In the resulting PC-space every spectrum of the dataset can be represented by a linear combination of these principal component vectors and also the spectra of pure components are part of the PC-space.

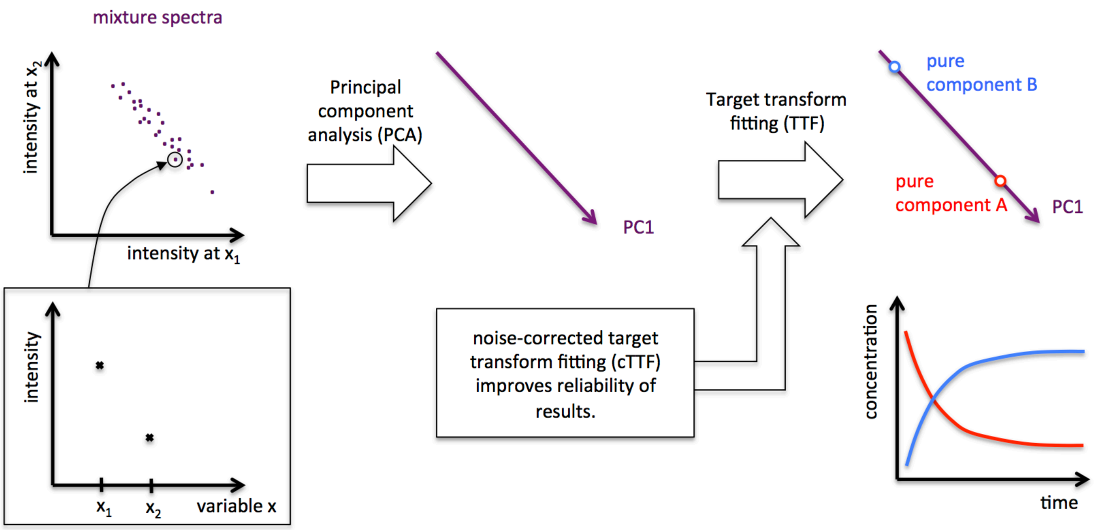

Figure 2:Illustration of the principles used in cTTF. Assumed is a bilinear set of mixture spectra. For n=2, each spectrum (of a series of spectra) consists of one intensity value at a variable x_1 and one intensity value at a variable x_2. Spectra can then be represented by a single point in a coordinate system with the axes (intensity at x_1) and (intensity at x_2). PCA evaluates, whether the data is well represented in a subspace of lower dimension. For the present example it finds a 1-dimensional subspace (PC1), indicating that mixture spectra consist of 2 components (A and B). The TTF algorithm determines the spectrum of pure component A and B, respectively. If spectra were e.g. recorded at various points in time, time profiles are obtained such as indicated here. If the initial dataset contains a lot of noise or components with low signal contribution, application of cTTF improves reliability of results.

TTF is an elaborate method to identify pure component spectra in the PC-space[41]. Besides, simpler approaches such as target factor analysis (TFA)[43] or iterative target

Physical Chemistry Chemical Physics Accepted Manuscript

Physical Chemistry Chemical Physics Accepted Manuscript

transform factor analysis (ITTFA)[44] are used for such purposes. Jandanklang *et al.*[41] - who introduced TTF - describe in detail how it is used to determine concentration profiles which follow a certain kinetic model in the PC-space. The application of TTF on the direct determination of pure component spectra follows the same principle, but has not been published before. In the following we will explain the 4 steps to identify pure component spectra in the PC-space with TTF:

(1) If the number of chemical components contributing to the mixture spectra is unknown, it can be determined from the number of principal components (PCs) necessary to represent the dataset sufficiently well. This number can e.g. be obtained from a scree plot (singular value plotted vs. principal component number), see Figure S2B. The number of pure component spectra is obtained by adding a value of 1 to the number of PCs.

(2) A suitable model for every pure component spectrum must be found, i.e. the shape and number of its individual signals. For many spectroscopic techniques Gaussians, Lorentzians or Voigt profiles are widely used to describe peak shapes.[45–49] Besides, a set of starting values for all signal parameters (e.g. peak position, width and Gaussian/Lorentzian mixing ratio) is needed. These starting values can be taken from a fit to an initial estimate of the pure spectrum obtained with ITTFA[44]. Alternatively, they can be given by the user as a rough estimate or from literature data.

(3) Like all spectra of the dataset, this synthetic start spectrum $\boldsymbol{t}$ is then represented by one point in the n-dimensional space. From this n-dimensional space it is projected into the PC-space.

(4) The distance d of the synthetic spectrum $\boldsymbol{t}$ (in the n-dimensional space) to its projection $\boldsymbol{t_{proj}}$ in the PC space is computed (mean-square-deviation)

$$d = |\boldsymbol{t} - \boldsymbol{t_{proj}}|$$

and then minimized by optimizing the parameters of the synthetic spectrum (peak widths, positions, intensities). This is performed by a non-linear optimization routine.

Key of this concept is that the distance *d* is minimal if the model spectrum is closest to a pure component spectrum in the PC-space, and the remaining distance can be considered as noise. This concept is reasonable because the model spectrum contains only the number of peaks absolutely necessary to reproduce pure component spectra. In contrast, mixture spectra have more signal peaks and are thus not well reproduced by the model spectrum, resulting in a large *d*. If *d* is minimal, $\boldsymbol{t}_{proj}$ is a good estimate of the spectrum of a pure component. We note that in general the application of TTF (and cTTF) is limited to data sets, in which the spectra of pure components can be well approximated by a small number of defined peaks.

In the following we describe how the fundamental noise distribution in the PC-space limits the performance of TTF and present cTTF as a method to circumvent these limitations. Experimental spectra typically carry some amount of noise which translates into noise on the position of every individual spectrum in the *n*-dimensional space. The PCs are computed to represent these noisy data points optimally. As a consequence, the direction of these PCs(exp.) is changed compared to the respective PCs(noise-free) of the corresponding hypothetical noise free dataset (Figure 3).

Physical Chemistry Chemical Physics Accepted Manuscript

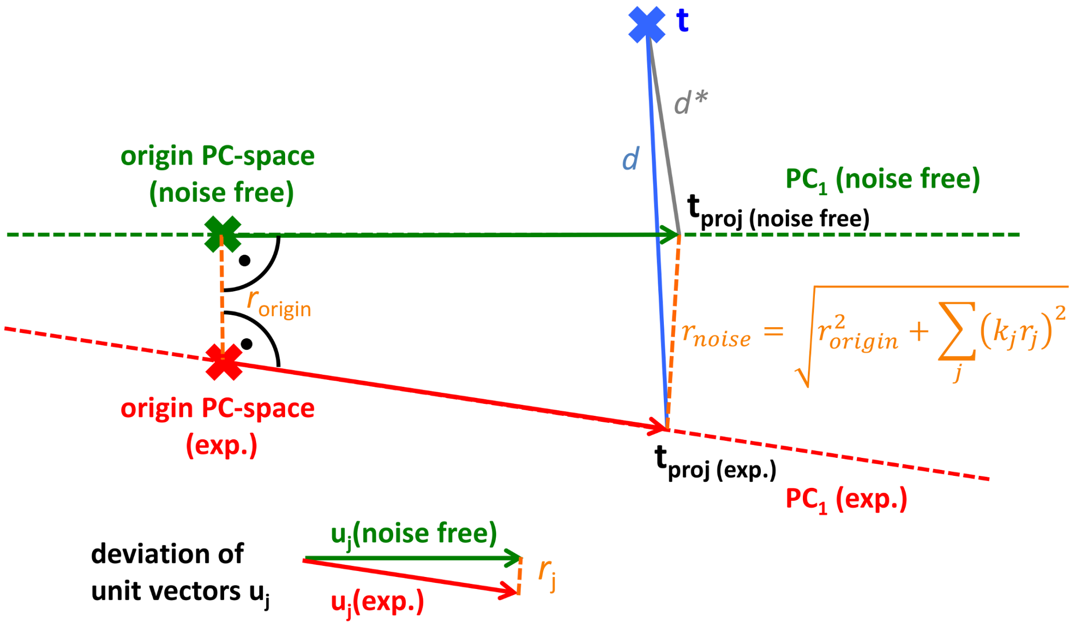

Figure 3:Schematic illustration of how noise in a dataset changes the direction of a PC(exp.) compared to the PC(noise free) of the corresponding hypothetical noise free dataset. The TTF routine minimizes the distance *d* between the model spectrum ***t*** and its projection $\boldsymbol{t_{proj}}$(exp.). As the model spectrum ***t*** is inherently noise-free, this minimization leads to a result (= pure component spectrum) which is biased towards the origin of the PC-space, since there the deviation between PCs(exp.) and PCs(noise-free) is minimal. cTTF corrects this bias by minimizing $d_{corr} = d / r_{noise}$.

TTF is thus most reliable if the deviation of PCs(exp.) and PCs(noise-free) is small. The reason is that the model spectrum ***t*** is inherently noise-free, but the TTF routine minimizes the distance *d* between ***t*** and its projection $\boldsymbol{t_{proj}}$(exp.), and not between ***t*** and $\boldsymbol{t_{proj}}$(noise-free). The distance *d* can also be described by the sum of the distance *d** between ***t*** and its projection $\boldsymbol{t_{proj}}$(noise-free) and the noise r_{noise} on the projection (Figure 3). In the case of significant noise r_{noise}, minimization of *d* leads to a result (= pure component spectrum) which is a compromise between minimizing both, *d** and

Physical Chemistry Chemical Physics Accepted Manuscript

Physical Chemistry Chemical Physics Accepted Manuscript

r_{noise}. Since r_{noise} is minimal at the origin of the PC-space, the pure component spectra will be biased towards the origin of the PC-space.

Here, we present cTTF as an extension of TTF, which corrects this problematic bias. In contrast to TTF, which minimizes the distance d between $\boldsymbol{t}$ and $\boldsymbol{t_{proj}}$(exp.), cTTF minimizes d_{corr}

$$d_{corr} = \frac{d}{r_{noise}} \tag{1}$$

By this, the TTF results are corrected by normalizing the determined residual d of the projection of the model spectrum by the amount of noise r_{noise} on the projection $\boldsymbol{t_{proj}}$(exp.). In the supporting information S4 we describe in detail how a model by Shabalin and Nobel[50] can be used to quantify r_{noise}. Besides, the advantage of cTTF compared to TTF is demonstrated on a simulated data set.

c) Application of cTTF to time-resolved photoelectron spectra

Here, we used two different datasets: one was recorded with a focus on the fast dynamics (delay time between pump and probe pulse Δt = -5 ps – 20 ps, Figure 1A), the other on slower dynamics (Δt = -5 ps – 1000 ps, Figure 1B). As the same species are expected to appear in both measurements, the datasets were analyzed together in order to reduce ambiguity in determining the spectra of these species[51–53].

The cTTF method requires the number of involved species. This number is reflected in the number of principal components describing the chemical transformations, which was determined by visual inspection of the measured spectra together with their projection into the PC-space. Two principal components were not enough to reproduce significant features in the spectra. With three principal components the spectra were well reproduced. A figure illustrating this decision can be found in the supporting information (Figure S5). As closure is present in this dataset a number of three principal components implies that four different states of water can be distinguished. In the next step, initial estimates for the spectra of these four species are needed. These were obtained with ITTFA[44] as described in the supporting information S6. Next, the four start spectra are fitted with a parametric model. A linear combination of a Gauss and a Lorentz function was used for each peak in the start spectrum. The only exception is the $1b_1$ peak in the gas phase. There, the asymmetric vibrational fine structure of this signal was considered with an additional peak. The parameters of this additional peak were fixed relative to the main $1b_1$-peak according to literature values (intensity ratio 1:5, energy distance 0.4 eV and same width)[54].

In photoelectron spectroscopy, inelastically scattered photoelectrons cause a background whose intensity increases towards higher binding energies. This was taken into account by the addition of a Tougaard-background[55] with a 2-parameter universal cross-section function.

Finally, noise-corrected cTTF delivers the spectra of pure species. Figure 4 summarizes the cTTF results and shows a good agreement of the final parametric model spectra $\boldsymbol{t}$ with their projections into the PC-space $\boldsymbol{t}_{proj}$. Based on literature data[29,36] on the photoelectron spectra of gas phase water, liquid water and on water clusters, we assign the four spectra to the pure component spectra of gas phase and liquid phase water and of small and large water clusters. Table 1 summarizes the parameters of the final model spectra $\boldsymbol{t}$ and compares them to literature values[29].

Physical Chemistry Chemical Physics Accepted Manuscript

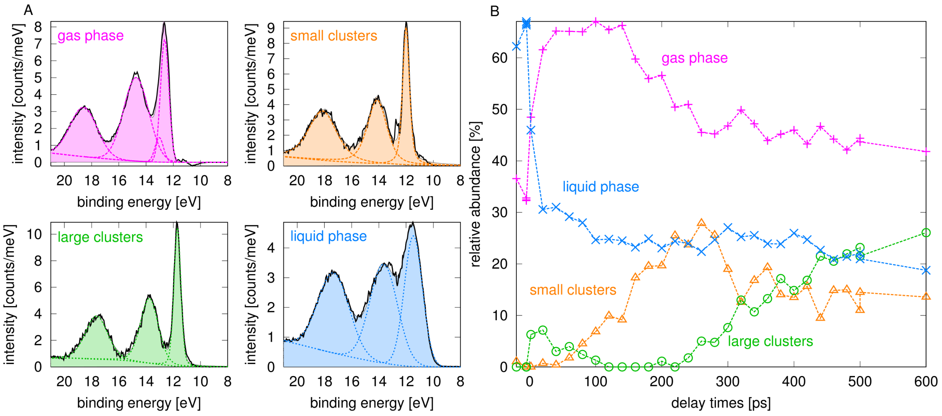

Figure 4:Spectra of pure components and their concentration profiles obtained from application of the cTTF method to the series of photoelectron spectra shown in Fig. 1.

A) Colored areas represent the final model spectrum for each of the four pure components. Dashed lines illustrate the peaks composing the model spectra. Solid black lines are the projections of the model spectra into the PC space. Based on literature data[29,36], the obtained spectra are assigned to gas phase water, liquid water, small and large water clusters.

B) The evolution of the relative contribution of gas, liquid, small and large cluster signal to every spectrum of the dataset (partly shown in Figure 1). Concentration profiles were constrained to non-negative values.

Physical Chemistry Chemical Physics Accepted Manuscript

Table 1: Final peak parameters

	E_{Bind} $1b_1$ [eV]	E_{Bind} $3a_1$ [eV]	E_{Bind} $1b_2$ [eV]	FWHM $1b_1$ [eV]	FWHM $3a_1$ [eV]	FWHM $1b_2$ [eV]
Gas	12.6	14.7±0.2	18.6±0.2	0.7	2.2	2.4
Gas Lit. [29]:	12.60	14.84±0.05	18.78±0.1	0.3	1.18	1.75
Small cluster	12.0±0.1	14.1±0.2	18.1±0.2	0.6	1.7	2.5
Large cluster	11.7±0.1	13.7±0.2	17.6±0.2	0.6	1.6	2.0
Liquid	11.4±0.15	13.6±0.2	17.3±0.2	1.6	2.4	2.7
Liquid Lit. [29]:	11.16±0.05	13.50±0.1	17.34±0.1	1.45	2.42	2.28

For the liquid phase spectrum, positions of spectral features and their widths are in agreement with literature data. Also in agreement are positions of gas phase signals. Photoelectron spectra of water clusters of different size have been recorded by Barth *et al.*[36]. They find an inverse proportional relationship between the cluster diameter and the position of the signal at lowest binding energy ($1b_1$ signal) relative to the respective liquid signal. Using their equation we roughly estimate the size of the small and large clusters to be on the order of 10 and 50 water molecules, respectively.

The width of the gas phase signals detected in our experiment is significantly broader than literature values and broader than the cluster signals detected in the same experiment. We explain this by the background pressure of water gas in the sample chamber and the fact that the focus of the XUV probe pulse is rather large (FWHM ~ 100 µm). Accordingly, the volume in which photoelectrons from gas phase molecules are generated is large and this initial space distribution impairs good resolution of the time-of-flight spectrometer. In contrast to this, the volume in which photoelectrons from the liquid and the clusters are generated is roughly confined to the dimension of the 20 µm diameter of the liquid jet, and their spectra are better

Physical Chemistry Chemical Physics Accepted Manuscript

Physical Chemistry Chemical Physics Accepted Manuscript

resolved.

Figure 4B displays the evolution of the contributions of gas, cluster and liquid signal for the dataset (-5 ps – 1000 ps). At negative delays, the spectra only contain liquid phase and gas phase signal. We distinguish three time regimes: (1) Within the first few ps, the contribution from the liquid strongly decreases, while the contribution of gas phase signal increases respectively. (2) Between about 50 ps and 150 ps, the signal contribution from gas phase water has its maximum and amounts to about 65%. Small clusters appear at ~ 50 ps and their signal contribution increases with time. (3) For times > 150 ps, the gas phase signal decreases, while the contribution of small clusters increases to its maximum contribution between 200 and 300 ps. It decreases for t > 300 ps, while the contribution of large clusters increases.

The contribution of liquid signal remains almost constant for t > 200 ps. We attribute this to a constant background signal of liquid water, resulting from the fact that IR pump and XUV probe focus have similar dimensions. A slight spatial mismatch may thus explain this constant background signal.

Besides, a small contribution from large clusters appears within a few ps and decays within 100 ps. We note, however, that this < 10% contribution is within the noise which we expect for the time profiles.

4 Discussion

In order to gain insight into the physical processes reflected in our observations and analysis we have used a simple fluid dynamics model to describe the expansion of supercritical water into vacuum. The model is based on equations from expansion wave theory. Figure 5A illustrates the initial state (t = 0 ps) of our model.

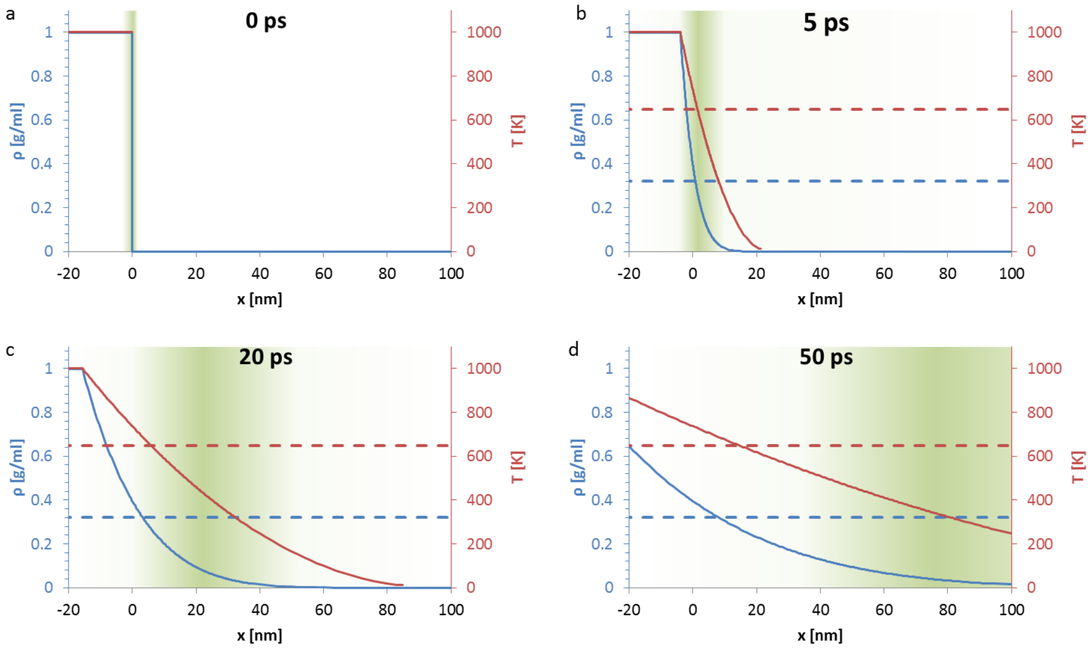

Figure 5:Density and temperature in the expanding system at various points in time. Dashed horizontal lines mark the critical density (red) and the critical temperature (blue). The green shaded area reflects the observation window of our experiment, which is confined by the limited escape depth of photoelectrons. The shading density illustrates the intensity of detected photoelectrons *I(d).*

The water - vacuum interface is defined as position x = 0 nm. In the initial state all water is at negative x-values, while vacuum is at positive x-values. The start temperature is T_0 = 1000 K and the start density of the supercritical water is ρ_0 = 1 g/ml. For the modeling of the expansion, water is approximated as an ideal gas with an

Physical Chemistry Chemical Physics Accepted Manuscript

adiabatic exponent $\gamma = 1.33$. The surface of the water jet is assumed to be flat. This is justified with the small distances (~ 100 nm) the particles travel during the 50 ps of the simulation. Heat flow and diffusion are neglected. In other words the expansion is adiabatic and the adiabatic relations for ideal gases apply. For this case, the temperature T and density ρ of the system can be obtained at all positions x and for all times t > 0 ps using the equation 2:

$$\sqrt{\frac{T}{T_0}} = \left(\frac{\rho}{\rho_0}\right)^{\frac{\gamma-1}{2}} = \frac{2}{\gamma+1}\left(1 - \frac{\gamma-1}{2}\frac{x}{a_0 t}\right) \tag{2}$$

x …….distance from the former surface of the liquid jet

t ……. time after excitation with the IR pulse

T …….temperature of the ideal gas as a function of x/t

ρ ….. density of the ideal gas as a function of x/t

T_0 …..temperature of the initial state fluid

ρ_0 …..density of the initial state fluid

γ …… adiabatic exponent of the ideal gas

a_0 …..speed of sound in the initial state fluid

Since we approximate water as an ideal gas, the speed of sound a_0 is obtained via:

$$a_0 = \sqrt{\gamma \frac{RT_0}{M}}\ . \tag{3}$$

R …… universal gas constant

M …..molar mass of the ideal gas

In the supporting information S7 we outline how equation 2 is derived. The results are presented in Figure 5. It shows the density profile and the temperature profile at various times during the expansion. The critical temperature ($T_c = 647$ K)[34] and the

Physical Chemistry Chemical Physics Accepted Manuscript

critical density ($\rho_c = 0.322$ g/ml)[34] are shown as dashed horizontal lines and allow to distinguish a supercritical state region and a subcritical state region.

In order to compare these results to the experimental data (Figures 1 and 4), we need two additional considerations: (1) Information on the probing depth of our experiment to estimate the region of the simulations which is observed in the experiment. (2) Information on how the changes in water density and temperature manifest themselves in the photoelectron spectrum.

(1) The probing depth is obtained via the electron attenuation length (EAL). The EAL is defined as the (shortest) distance from a starting point A to an arrival point B, at which the initial photoelectron signal I_0 is reduced to $I = I_0/e$. Only photoelectrons generated within this distance to the material surface significantly contribute to the structured part of the photoelectron spectrum. Recent liquid jet experiments by Thürmer *et al.*[56] and Suzuki *et al.*[57] suggest an EAL on the order of 1 nm for photoelectron kinetic energies between 15 - 30 eV (in our experiment hν = 38 eV and electron binding energies range from ~10 - 25 eV). This implies that the experiment only detects photoelectron signals from the first few layers of water at t = 0 ps and from the forefront of the expansion for t > 0 ps. To model the detection probability of photoelectrons created at a position *d* along the x-axis, we assume that for bulk water density ρ_0 the $EAL_0 = 1$ nm. For other densities ρ it is $EAL = EAL_0\ (\rho_0 / \rho)$. For all positions *d* along the x-axis, the intensity *I(d)* of detected photoelectrons, and accordingly the overall signal contribution of this position *d* to the photoelectron spectrum, is then proportional to:

$$I(d) \propto \rho(d)\ exp\left(-\frac{\int_d^\infty \rho(x)dx}{\rho_0\ EAL_0}\right) \qquad (4)$$

Physical Chemistry Chemical Physics Accepted Manuscript

ρ(d) is the density at the position of interest *d*. It is assumed to be proportional to the intensity of photoelectrons generated at this position. The integral $\int \rho(x)\,dx$ is the integral over the density from the forefront of the expansion up to the position *d*. The result is visualized as shaded areas in Figure 5. Dark shaded areas mark high signal contributions to the overall photoelectron spectrum and light shaded areas mark low signal contribution.

(2) Figure 5 illustrates that temperature and pressure in the observation volume drop to approximately the critical values within the first 5 ps, and clearly below them within 20 ps. In order to compare this to our experimental data, we need information on how the photoelectron spectrum changes with a change in water density and temperature. This information is not directly available. However, Winter and Faubel[30] suggest that the main reason for the lower binding energy of liquid phase photoelectron signals compared to the respective gas phase signals is a result of stabilization of the ionized species by the surrounding water molecules in the liquid. This stabilization decreases with decreasing density, and a drop in density is thus expected to result in an increase in binding energies of photoelectron signals. The amount of stabilization can be estimated from the polarization contribution of the Born model of solvation[30]. It depends on the optical macroscopic dielectric constant of water ε_{opt}, which can be determined from the index of refraction $\varepsilon_{opt} = n^2$. The difference in binding energy ΔE between a signal in the gas and liquid phase is then proportional to $\Delta E \propto (1 - 1/\varepsilon_{opt})$. For liquid water $\varepsilon_{opt}(300\ \mathrm{K}, 1\ \mathrm{g/ml}) = 1.8$[58] and predicts $\Delta E = 1.4$ eV, in agreement with experimental findings[30]. For conditions around the critical point $\varepsilon_{opt}(647\ \mathrm{K}, 0.322\ \mathrm{g/ml}) = 1.2$[58] and predicts a significantly smaller $\Delta E = 0.5$ eV. This simple approach illustrates that a decrease in density manifests itself in a shift of photoelectron signals towards higher binding energies.

Physical Chemistry Chemical Physics Accepted Manuscript

With this information, results from fluid dynamics simulations (Fig. 5) can be compared to experimental data (Fig. 1) and cTTF results (Fig. 4). This leads to the following picture:

(1) Within the first 5 ps of the expansion the density in the observation volume of our experiment drops to values around the critical point.

As outlined above, this decrease in density directly translates into an increase in electron binding energy. Accordingly, in the spectra from 2 ps to 20 ps (Figure 1A), the center of the $1b_{1,liq}$ signal is shifted towards higher binding energies with respect to the reference spectrum at -5 ps. The decrease in density also manifests itself in the cTTF results of Figure 4 as the significant drop in liquid signal contribution and the respective increase in gas phase contribution within the first 20 ps.

The origin of the small transient signal (contribution < 10%) from large clusters, visible in the cTTF results between a few ps and 100 ps, is within the noise expected for the time profiles. However, such a signal might result from an inhomogeneous deposition of energy in the observation volume. Certainly, the expansion is not perfectly homogeneous, rendering a transient appearance of liquid water fragments reasonable.

(2) From 5 ps to about 20 ps the volume further expands while temperature and density in the observation volume drop significantly below the critical values, leading to formation of water clusters via condensation.

When temperature and density drop below the critical values, a supersaturated phase emerges. Figure 6 shows the average supersaturation in the observation volume as a function of time.

Physical Chemistry Chemical Physics Accepted Manuscript

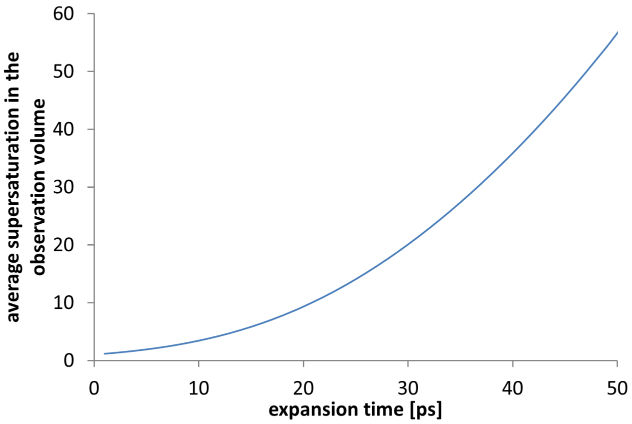

Figure 6:Average supersaturation in the observation volume of our photoelectron spectroscopy experiment as a function of time. The supersaturation was calculated from the mean densities and temperatures in the observation volume.

Fransen *et al.*[59] report that significant formation of condensation seeds is observed within 500 µs for supersaturations between 8 and 13 at densities of about 5 g/m³. We note that extrapolation of this data to the conditions present in our experiment (density = 0.1 g/ml, supersaturation = 13) suggests that formation of condensation seeds takes place on the few ps-timescale, as the time constant for formation of seeds scales with $1/\rho^2$. In our fluid dynamics simulation a supersaturation of 13 is reached at t = 24 ps, and formation of seeds is thus expected several picoseconds afterwards. This timescale is surprisingly consistent with the appearance of small clusters in the cTTF results at t ~ 50 ps and the subsequent increase of their contribution. For t > 150 ps, the cluster signal contribution is strong enough to be directly visible in the photoelectron spectra as a shoulder on the low binding energy side of the $1b_{1,g}$ signal. cTTF results further show that condensation into clusters is going along with a decay in gas phase contribution for t > 150 ps, as would be expected.

Physical Chemistry Chemical Physics Accepted Manuscript

(3) In the further course of the expansion (t > 150 ps), the clusters size increases.

The cTTF results illustrate this by a decrease in signal contribution from small clusters (~10 water molecules; size estimated with Ref.[36]) and an increase in signal from large clusters (~50 water molecules[36]) occurring between 200 – 600 ps. We note that the gas phase does not significantly decrease within this time window, indicating that larger clusters form according to predictions of condensation theory. The evolution of the cluster signal can also directly be seen in the photoelectron spectra.

With this, the unique combination of experiment, data analysis and simulation presented here delivers a comprehensive picture on the ultrafast expansion dynamics of supercritical water. It further demonstrates that the initial dynamics (t < 50 ps) of the expanding phase are well described by a simple fluid dynamics simulation. The timescales of the simulation are in good agreement with experimental results.

We note that the presented results complete the work on the ultrafast dynamics of superheated water, which has previously been published by our group, but was primarily focused on a qualitative description of the obtained experimental data[17–20]. The reason lies in the complexity of the spectra featuring strong overlap of photoelectron signals from water gas, liquid and clusters. Only the cTTF method presented here allowed us to disentangle the spectra and to access consolidated information on the expansion mechanism and timescales.

Our work ties up to the recent study of Franjic and Miller[21]. They prepared highly excited thermodynamic water phases at the water/air interface with an IR-laser (2960 nm) pulse, and investigated the macroscopic expansion for timesclaes > 100 ps via time-resolved dark-field imaging and time-resolved optical reflectivity[21]. Their experiment captures dynamics on timescales ranging from a few 100 ps to several

Physical Chemistry Chemical Physics Accepted Manuscript

microseconds, and the observed length scales of the expansion are on the micrometer scale.

Our experiment adds significant detail to this picture, as it captures the ultrafast dynamics on the few picosecond timescale. In addition, the surface sensitivity of photoelectron spectroscopy confines the measurements to an observation window with a thickness on the nanometer scale. With this, we selectively monitor the expansion of a thin and almost homogeneously heated, supercritical phase of water. In constrast to this, Franjic and Miller detect signal from the entire ensemble of water heated by the IR laser pulse[21]. As the IR light is almost completely absorbed within a few micrometers from the water surface, this ensemble comprises supercritical water at and near the surface and subcritical water from deeper water layers. Franjic and Miller claim that this ensemble can be described by a metastable liquid phase which separates into gas and liquid phase via a spinodal decomposition[21]. This is in contrast to our observation, in which the water expands to values below the critical density and temperature, and subsequent condensation is observed. Further experiments are needed to ascertain if this difference is caused by the different IR-pulse lengths: 100 ps in the experiment of Franjic and Miller[21], and 250 fs in the experiment presented here. However, as the fluences in the experiment of Franjic and Miller (0.2 - 1 J/cm^2) are comparable to our value (0.25 J/cm^2), dynamics of surface water layers might even be identical in both experiments; but only the surface sensitivity of our experiment allows to selectively monitor them.

Physical Chemistry Chemical Physics Accepted Manuscript

Physical Chemistry Chemical Physics Accepted Manuscript

5 Summary and conclusions

We present time-resolved photoelectron spectra on the ultrafast expansion dynamics of supercritical water into vacuum. The series of photoelectron spectra was successfully analyzed with noise-corrected target transform fitting (cTTF), a specifically developed multivariate method based on target transform fitting (TTF). The strength of the method lies in extracting the spectra of pure components out of a series of mixture spectra. We demonstrate that cTTF delivers reliable results even for complex spectra consisting of three and more chemical species each contributing multiple peaks to the mixture spectrum. In general, we expect the cTTF algorithm to work particularly well for spectra consisting of individual, well defined peak forms, as found in photoelectron, X-ray absorption, Raman, IR or NMR spectra. In the presented case, cTTF reveals four components (gas, liquid, small clusters, large clusters), their spectra, and their time profiles during the expansion process. With this, cTTF results provide unprecedented quantitative information on the expansion dynamics of supercritical water: the involved water species and the time scales they appear.

Together with a simple fluid dynamics simulation, a comprehensive picture emerges: When water is heated up to temperatures above the critical point with an ultrashort laser pulse, subsequent expansion dynamics take place on picosecond timescales. For the case of expansion of the supercritical phase into vacuum, temperature and density of the expanding phase drop below the critical values on a few picosecond timescale. This results in a supersaturated phase, in which condensation seeds form within t ~ 50 ps and grow from small clusters to large clusters on the few 100 ps timescale.

With the above results, the work presented here delivers new insights into the ultrafast dynamics of water under extreme conditions and provides a link between ultrafast energy relaxation experiments of vibrationally excited water molecules taking place on the 1 ps timescale[8,9,11,13–16] and experiments on the macroscopic expansion of highly excited thermodynamic water phases reported for timescales > 100 ps[21].

The combined experimental and theoretical approach presented here may be relevant for better understanding differences in the ablation mechanisms in laser induced liquid beam ionization/desorption (LILBID) mass spectrometry[25,26] and matrix-assisted laser desorption/ionization (MALDI) from water ice matrices[23,24].

It also opens up an experimental route towards understanding dynamics of other hydrogen bond networks under extreme conditions and their differences compared to water[20]. Besides, it demonstrates that time-resolved XUV photoelectron spectroscopy on liquids will be a powerful tool for future studies on the ultrafast dynamics of liquids. In such experiments, the surface sensitivity of photoelectron spectroscopy might be exploited to confine the measurements to an observation window within a few nanometers from the surface and thus to obtain specific spatial information in addition to temporal resolution.

Acknowledgements

The authors thank the Deutsche Forschungsgemeinschaft and the European Social Fund for financial support through the SFB/TRR 102 and the NFG Echem, respectively.

We also thank Anika Gladytz, Dr. Oliver Link and Dr. E. Lugovoy for experimental support and insightful discussions. This work made use of the free software package GNU Octave, and the authors are grateful for the support of the Octave development community.

Physical Chemistry Chemical Physics Accepted Manuscript

References

1. P. Wernet, D. Nordlund, U. Bergmann, M. Cavalleri, M. Odelius, H. Ogasawara, L. Å. Näslund, T. K. Hirsch , L. Ojamäe, P. Glatzel, L. G. M. Pettersson and A. Nilsson, *Science*, 2004, **304**(5673), 995.
2. A. Nilsson and L. G. M. Pettersson, *Chem. Phys.*, 2011, **389**(1–3), 1.
3. T. D. Kühne and R. Z. Khaliullin, *Nat. Commun*, 2013, **4**, 1450.
4. C. J. Sahle, C. Sternemann, C. Schmidt, S. Lehtola, S. Jahn, L. Simonelli, S. Huotari, M. Hakala, T. Pylkkänen, A. Nyrow, K. Mende, M. Tolan, K. Hämäläinen and M. Wilke, *Proc. Nat. Acad. Sci.*, 2013, **110**(16), 6301.
5. D. Lis, E. H. G. Backus , J. Hunger, S. H. Parekh and M. Bonn, *Science*, 2014, **344**(6188), 1138.
6. M. D. Baer, C. J. Mundy, M. J. McGrath, I.-F. W. Kuo, J. I. Siepmann and D. J. Tobias, *Chem. Phys.*, 2011, **135**, 124712.
7. R. Vácha, O. Marsalek, A. P. Willard, D. J. Bonthuis, R. R. Netz and P. Jungwirth, *J. Phys. Chem. Lett.*, 2011, **3**(1), 107.
8. M. L. Cowan, B. D. Bruner, N. Huse, J. R. Dwyer, B. Chugh, E. T. J. Nibbering, T. Elsaesser and Miller, R. J. D., *Nature*, 2005, **434**(7030), 199.
9. K. Ramasesha, L. de Marco, A. Mandal and A. Tokmakoff, *Nat Chem*, 2013, **5**(11), 935.
10. M. Olschewski, S. Knop, J. Lindner and P. Vöhringer, *Angew. Chem. Int. Ed.*, 2013, **52**(37), 9634.
11. C.-S. Hsieh, M. Okuno, J. Hunger, Ellen H. G. Backus, Y. Nagata and M. Bonn, *Angew. Chem. Int. Ed.*, 2014, **53**(31), 8146.

Physical Chemistry Chemical Physics Accepted Manuscript

12. J. A. Sellberg, C. Huang, T. A. McQueen, N. D. Loh, H. Laksmono, D. Schlesinger, R. G. Sierra, D. Nordlund, C. Y. Hampton, D. Starodub, D. P. DePonte, M. Beye, C. Chen, A. V. Martin, A. Barty, K. T. Wikfeldt, T. M. Weiss, C. Caronna, J. Feldkamp, L. B. Skinner, M. M. Seibert, M. Messerschmidt, G. J. Williams, S. Boutet, L. G. M. Pettersson, M. J. Bogan and A. Nilsson, *Nature*, 2014, **510**(7505), 381.
13. A. Pakoulev, Z. Wang and D. D. Dlott, *Chem. Phys. Lett.*, 2003, **371**(5–6), 594.
14. J. Lindner, P. Vöhringer, M. S. Pshenichnikov, D. Cringus, D. A. Wiersma and M. Mostovoy, *Chem. Phys. Lett.*, 2006, **421**(4–6), 329.
15. T. Schäfer, J. Lindner, P. Vöhringer and D. Schwarzer, *Chem. Phys.*, 2009, **130**(22), 224502.
16. K. L. Vodopyanov, *Chem. Phys.*, 1991, **94**(8), 5389.
17. O. Link, E. Vöhringer-Martinez, E. Lugovoj, Y. Liu, K. Siefermann, M. Faubel, H. Grubmüller, R. B. Gerber, Y. Miller and B. Abel, *Faraday Discuss.*, 2009, **141**, 67.
18. O. Link, E. Lugovoy, K. Siefermann, Y. Liu, M. Faubel and B. Abel, *Appl. Phys. A*, 2009, **96**(1), 117.
19. M. Faubel, K. R. Siefermann, Y. Liu and B. Abel, *Acc. Chem. Res.*, 2011, **45**(1), 120.
20. E. Vohringer-Martinez, O. Link, E. Lugovoy, K. R. Siefermann, F. Wiederschein, H. Grubmuller and B. Abel, *Phys. Chem. Chem. Phys.*, 2014, **16**(36), 19365.
21. K. Franjic and R. J. D. Miller, *Phys. Chem. Chem. Phys.*, 2010, **12**(20), 5225.
22. A. Vogel and V. Venugopalan, *Chem. Rev.*, 2003, **103**(2), 577.
23. S. Berkenkamp, M. Karas and F. Hillenkamp, *P. Natl. Acad. Sci. USA*, 1996, **93**(14), 7003.
24. A. Pirkl, J. Soltwisch, F. Draude and K. Dreisewerd, *Anal. Chem.*, 2012, **84**(13), 5669.
25. A. Wattenberg, F. Sobott, H.-D. Barth and B. Brutschy, *Int. J. Mass Spectrom.*, 2000, **203**(1–3), 49.

Physical Chemistry Chemical Physics Accepted Manuscript

26. B. Abel, A. Charvat, U. Diederichsen, M. Faubel, B. Girmann, J. Niemeyer and A. Zeeck, *Int. J. Mass Spectrom.*, 2005, **243**(2), 177.

27. E. Rapp, A. Charvát, A. Beinsen, U. Plessmann, U. Reichl, A. Seidel-Morgenstern, H. Urlaub and B. Abel, *Anal. Chem.*, 2008, **81**(1), 443.

28. U. Emmerichs, S. Woutersen and H. J. Bakker, *J. Opt. Soc. Am. B*, 1997, **14**(6), 1480.

29. B. Winter, R. Weber, W. Widdra, M. Dittmar, M. Faubel and Hertel, IV, *J. Phys. Chem. A*, 2004, **108**(14), 2625.

30. B. Winter and M. Faubel, *Chem. Rev.*, 2006, **106**(4), 1176.

31. D. M. Wieliczka, S. Weng and M. R. Querry, *Appl. Opt.*, 1989, **28**(9), 1714.

32. A. Vogel, J. Noack, K. Nahen, D. Theisen, S. Busch, U. Parlitz, D. X. Hammer, G. D. Noojin, B. A. Rockwell and R. Birngruber, *Appl. Phys. B*, 1999, **68**(2), 271-280.

33. NIST Chemistry Webbook: Thermophysical Properties of Fluid Systems, http://webbook.nist.gov/chemistry/fluid/, (accessed October 2014).

34. W. Wagner and A. Pruß, *J. Phys. Chem. Ref. Data*, 2002, **31**(2), 387.

35. Note: We note that the NIST Chemistry Webbook only provides data up to pressures of 1GPa, which is reached at a temperature of ca. 800 K and a deposited energy of 30 kJ/mol. To estimate the temperature after further depoosition of the remaining 10 kJ/mol, the heat capacity c = 50 J/(molK) is used and assumed to stay constant.

36. S. Barth, M. Ončák, V. Ulrich, M. Mucke, T. Lischke, P. Slavíček and U. Hergenhahn, *J. Phys. Chem. A*, 2009, **113**(48), 13519.

37. O. Björneholm, F. Federmann, S. Kakar and T. Möller, *J. Chem. Phys.*, 1999, **111**(2), 546.

38. G. Öhrwall, R. F. Fink, M. Tchaplyguine, L. Ojamäe, M. Lundwall, R. R. T. Marinho, A. Naves de Brito, S. L. Sorensen, M. Gisselbrecht, R. Feifel, T. Rander, A. Lindblad,

Physical Chemistry Chemical Physics Accepted Manuscript

J. Schulz, L. J. Saethre, N. Martensson, S. Svensson and O. Björneholm, *J. Chem. Phys.*, 2005, **123**(5), 054310.

39. A. de Juan, M. Maeder, M. Martínez and R. Tauler, *Chemom. Intell. Lab. Syst.*, 2000, **54**(2), 123.
40. C. Ruckebusch, M. Sliwa, J. Réhault, P. Naumov, J. P. Huvenne and G. Buntinx, *Anal. Chim. Acta*, 2009, **642**(1–2), 228.
41. P. Jandanklang, M. Maeder and A. C. Whitson, *J. Chemom.*, 2001, **15**(6), 511.
42. S. Wold, K. Esbensen and P. Geladi, *Chemom. Intell. Lab. Syst.*, 1987, **2**(1), 37.
43. E. R. Malinowski, *Anal. Chim. Acta*, 1978, **103**(4), 339.
44. B. G. M. Vandeginste, W. Derks and G. Kateman, *Anal. Chim. Acta*, 1985, **173**(0), 253.
45. S. Evans, *Surf. Interface Anal.*, 1991, **17**(2), 85.
46. S. Kundu, Y. Wang, W. Xia and M. Muhler, *J. Phys. Chem. C*, 2008, **112**(43), 16869.
47. O. Rosseler, M. Sleiman, V. N. Montesinos, A. Shavorskiy, V. Keller, N. Keller, M. I. Litter, H. Bluhm, M. Salmeron and H. Destaillats, *J. Phys. Chem. Lett.*, 2013, **4**(3), 536.
48. M. S. Dresselhaus, A. Jorio, M. Hofmann, G. Dresselhaus and R. Saito, *Nano Lett.*, 2010, **10**(3), 751.
49. P. Dlapa, M. B. Bodí, J. Mataix-Solera, A. Cerdà and S. H. Doerr, *CATENA*, 2013, **108**(0), 35.
50. A. A. Shabalin and A. B. Nobel, *J. Multivariate Analysis*, 2013, **118**(0), 67.
51. C. Ruckebusch, M. Sliwa, P. Pernot, A. de Juan and R. Tauler, *J. Photochem. Photobiol. C*, 2012, **13**(1), 1.
52. M. Amrhein, B. Srinivasan, D. Bonvin and M. M. Schumacher, *Chemom. Intell. Lab. Syst.*, 1996, **33**(1), 17.

Physical Chemistry Chemical Physics Accepted Manuscript

53. K.-H. Müller and T. Plesser, *Eur. Biophys. J.*, 1991, **19**(5), 231.

54. C. R. Brundle and D. W. Turner, *Proc. Roy. Soc. A.*, 1968, **307**(1488), 27.

55. S. Tougaard and P. Sigmund, *Phys. Rev. B*, 1982, **25**(7), 4452.

56. S. Thürmer, R. Seidel, M. Faubel, W. Eberhardt, J. C. Hemminger, S. E. Bradforth and B. Winter, *Phys. Rev. Lett.*, 2013, **111**(17), 173005.

57. Y.-I. Suzuki, K. Nishizawa, N. Kurahashi and T. Suzuki, *Phys. Rev. E*, 2014, **90**(1), 10302.

58. A. H. Harvey, J. S. Gallagher and J. M. H. L. Sengers, *J. Phys. Chem. Ref. Data*, 1998, **27**(4), 761.

59. M. A. L. J. Fransen, E. Sachteleben, J. Hrubý and D. M. J. Smeulders, *Exp. Fluids*, 2014, **55**(7), 1-17.

Physical Chemistry Chemical Physics Accepted Manuscript